

# RSC Advances



This is an *Accepted Manuscript*, which has been through the Royal Society of Chemistry peer review process and has been accepted for publication.

*Accepted Manuscripts* are published online shortly after acceptance, before technical editing, formatting and proof reading. Using this free service, authors can make their results available to the community, in citable form, before we publish the edited article. This *Accepted Manuscript* will be replaced by the edited, formatted and paginated article as soon as this is available.

You can find more information about *Accepted Manuscripts* in the [Information for Authors](#).

Please note that technical editing may introduce minor changes to the text and/or graphics, which may alter content. The journal's standard [Terms & Conditions](#) and the [Ethical guidelines](#) still apply. In no event shall the Royal Society of Chemistry be held responsible for any errors or omissions in this *Accepted Manuscript* or any consequences arising from the use of any information it contains.

**A Novel hydrolytic reaction to morphology-controlled TiO<sub>2</sub>  
micro/nanostructures for enhanced photocatalytic performances**

He Cheng<sup>1,2a</sup>, Gongde Chen<sup>1,2a</sup>, Weixin Zhang<sup>1,2,\*</sup>, Maoqin Qiu<sup>1,2</sup>, Zeheng Yang<sup>1,2</sup>,

Xiao Zhu<sup>1,2</sup>, Guo Ma<sup>1,2</sup>, and Yu Fu<sup>1</sup>

<sup>1</sup>School of Chemistry and Chemical Engineering, Hefei University of Technology,

Hefei, Anhui 230009, PR China

<sup>2</sup>Anhui Key Laboratory of Controllable Chemical Reaction & Material Chemical

Engineering, Hefei, Anhui 230009, PR China

<sup>a</sup>These authors are co-first authors, who contributed equally to this work.

---

\*Corresponding author

Tel.: 86-551-62901450; Fax: 86-551-62901450

E-mails: wxzhang@hfut.edu.cn, (Weixin Zhang)

## Abstract

Different TiO<sub>2</sub> micro/nanostructures have been hydrothermally prepared through controlling hydrolysis and nucleation rate of Ti<sup>4+</sup> ions by urea and H<sub>2</sub>O<sub>2</sub> in (NH<sub>4</sub>)<sub>2</sub>TiF<sub>6</sub> aqueous solution. Anatase TiO<sub>2</sub> nanorods with diameters of 10-30 nm and lengths up to 300-500 nm were evolved from the intermediate monoclinic H<sub>2</sub>Ti<sub>5</sub>O<sub>11</sub>·3H<sub>2</sub>O in the presence of H<sub>2</sub>O<sub>2</sub> and urea whereas TiO<sub>2</sub> core-shell nanospheres with diameters of 300-500 nm were obtained with the sole assistance of urea via Ostwald ripening effect and TiO<sub>2</sub> microspheres with diameters of about 1-2 μm were formed in the presence of only H<sub>2</sub>O<sub>2</sub>. Photocatalytic degradation of Rhodamine B (RhB) has been used to evaluate their activities. The results indicate that the anatase TiO<sub>2</sub> nanorods have superior photocatalytic efficiency to the core-shell nanospheres and microspheres counterparts owing to their larger specific surface area and higher yield of ·OH radicals. This work not only offers a simple and promising route to controllable synthesis of various TiO<sub>2</sub> architectures, but also provides a new insight for improving photocatalytic performance of TiO<sub>2</sub> through morphological engineering, which will expect potential applications in environmental remediation.

**Keywords:** Hydrolysis; TiO<sub>2</sub>; Ostwald ripening; Rhodamine B; Photocatalysis.

## 1. Introduction

Engineering the morphology of TiO<sub>2</sub> nanostructures has been recognized as a promising strategy to drive their potential applications in photocatalysis, sensing, photoelectric conversion, etc.<sup>1-5</sup> As one of the most promising photoactive materials, TiO<sub>2</sub> with large surface areas, excellent charge separation and mobility, and strong light absorption capacity are highly desirable for photocatalysis given the advantages of more active sites and increased quantum efficiency.<sup>6,7</sup>

In the past decades, extensive studies have been devoted to synthesize TiO<sub>2</sub> nanostructures with various morphologies, some of which have been demonstrated with exceptional photocatalytic activity.<sup>8-11</sup> Among them, TiO<sub>2</sub> nanorods and core-shell nanospheres have attracted much attention because of their enhanced photocatalytic performances resulted from the remarkable decrease in recombination rate of photogenerated carriers due to delocalization of electrons in 1-D nanostructures and enhanced light harvesting ability through multiple light scattering and reflection within core-shell structures and a large number of active sites provided for the reactions.<sup>12,13</sup> For instance, Yi and coworkers synthesized TiO<sub>2</sub> nanorods with high aspect ratio by sol-gel method with the assistance of surfactants. The TiO<sub>2</sub> nanorods showed superior photo-oxidation efficiency for formic acid than nanoparticles due to the decrease of probability of e<sup>-</sup>/h<sup>+</sup> recombination.<sup>12</sup> Guo *et al.* prepared core-shell TiO<sub>2</sub> microspheres by template-assisted solvothermal alcoholysis with subsequent calcination. The prepared core-shell materials exhibited significantly greater efficiency in the photodecomposition of RhB than P25 because of their larger

surface area and more efficient use of light through multiple reflection.<sup>14</sup>

In order to achieve shape-controlled TiO<sub>2</sub> photocatalysts, approaches based on sol-gel process, hydrothermal and solvothermal synthesis have been proposed.<sup>15-18</sup> Hyeon *et al.*<sup>19</sup> synthesized anatase TiO<sub>2</sub> nanorods with a diameter of 3.4 nm and a length of 38 nm using a non-hydrolytic sol-gel reaction between titanium (IV) isopropoxide and oleic acid with 1-hexadecylamine for diameter control at 270 °C. Teng *et al.*<sup>20</sup> prepared anatase TiO<sub>2</sub> nanorods through hydrothermal treatment of TiO<sub>2</sub> nanotubes under an acid condition based on local shrinkage of nanotubes and oriented attachment of anatase crystallites. Fujishima *et al.*<sup>21</sup> prepared mesoporous core-shell TiO<sub>2</sub> spheres by electrospray of N-vinyl-2-pyrrolidone and titanium butoxide sol and subsequent hydrothermal treatment. Lu *et al.*<sup>13</sup> prepared sphere-in-sphere TiO<sub>2</sub> structures through solvothermal treatment of TiOSO<sub>4</sub> in glycerol, alcohol, and ethyl ether.

However, some limitations have been confronted by current reaction systems, such as using organic solvent and surfactant, and experiencing multi-step treatment from precursor to final products. It is still a big challenge to controllably prepare a variety of TiO<sub>2</sub> structures simultaneously in one reaction system. For practical application, it is highly desirable to develop a flexible and robust reaction system in which a variety of TiO<sub>2</sub> structures can be selectively prepared merely through adjusting reaction parameters.

Herein, a novel hydrolytic reaction system based on one-pot hydrothermal method has been successfully developed to controllably prepare anatase TiO<sub>2</sub> with

three different micro/nanostructures: nanorods, core-shell nanospheres and microspheres. Morphologies of  $\text{TiO}_2$  were tailored through tuning hydrolysis and nucleation rate of  $\text{Ti}^{4+}$  by the addition of urea and  $\text{H}_2\text{O}_2$ . Photocatalytic degradation of RhB aqueous solution served as the probe reaction to compare their catalytic performances. This work proposes a flexible and robust pathway for large-scale preparation of a variety of  $\text{TiO}_2$  structures in one reaction system and provides promising candidates for waste water treatment.

## 2. Experimental section

### 2.1. Materials

All chemicals including  $(\text{NH}_4)_2\text{TiF}_6$  (98.0 wt%), urea ( $\geq 99.0$  wt%), and  $\text{H}_2\text{O}_2$  (30 wt%) were purchased from Sinopharm Chemical Reagent Co., Ltd, China and used as-received without any further purification.

### 2.2. Synthesis of $\text{TiO}_2$ samples

5 mL of  $\text{H}_2\text{O}_2$  was mixed with 30 mL of  $(\text{NH}_4)_2\text{TiF}_6$  aqueous solution (0.02 mol/L). Then 3 g of urea was dissolved in the above solution and the obtained solution was subsequently transferred into a 60 mL Teflon-lined stainless steel autoclave. After being heated in an oven at 180 °C for 2 h, sample A was collected, washed with distilled water and ethanol for three times, respectively, and dried in the oven at 60 °C overnight. Sample B and C were synthesized by following a similar procedure as sample A, but the difference is that sample B was prepared with the sole assistance of urea and sample C with the sole assistance of  $\text{H}_2\text{O}_2$ .

### 2.3. Catalyst characterization

The samples were characterized by X-ray powder diffraction (XRD) on a Rigaku D/max- $\gamma$ B X-ray diffractometer with a Cu  $k\alpha$  radiation source ( $\lambda=0.154178$  nm), operated at 40 kV and 80 mA. The scanning time of XRD measurement for every sample was 15 min, and the step width was 0.02 degree. The morphologies and structures of the samples were measured on field-emission scanning electron microscope (FESEM, FEI Sirion-200) and high resolution transmission electron microscope (HRTEM) (JEM-2100F) at an accelerating voltage of 200 kV. Photoluminescence (PL) spectra were recorded at room temperature on a fluorescence spectrophotometer (Hitachi F-4500) with a Xenon lamp (150 W) as the excitation source. Both entrance and exit slits were 5.0 nm and the scanning speed was 1200 nm/min. Diffuse reflectance UV-visible spectra within a wavelength range of 200-800 nm were recorded on a Shimadzu 2550 UV-visible spectrometer and BaSO<sub>4</sub> powder was used as the internal standard. Fourier transform infrared spectroscopy (FTIR) analysis was carried out on SHIMAZU IR440 spectrometer in the range of 500-4000 cm<sup>-1</sup>.

N<sub>2</sub> adsorption-desorption isotherms were recorded on a Quantachrome NOVA 2200e surface area and pore size analyzer at liquid nitrogen temperature. All samples were degassed at 120 °C for 4 h prior to measurements. The specific surface area of the samples was calculated by following the multipoint Brunauer–Emmett–Teller (BET) procedure, and the average pore diameter was determined by the Barrett–Joyner–Halenda (BJH) method using the desorption isothermal.

#### **2.4. Photocatalytic activity measurement**

The photocatalytic degradation of RhB was performed in a cylindrical quartz reactor of 7 cm × 9 cm (diameter × height). The solution in the reaction was agitated using a magnetic bar. A high-pressure Hg lamp (predominant wavelength  $\lambda=365$  nm, 300 W) was used as the light source and placed in a quartz jacket with a water circulation to cool the lamp. The distance between the lamp and reactor is 10 cm. Typically, 0.05 g of samples were dispersed in 100 mL of RhB aqueous solution with an initial concentration of  $1 \times 10^{-5}$ ,  $2 \times 10^{-5}$  and  $5 \times 10^{-5}$  mol/L, respectively, and then magnetically stirred in the dark for 2 h to reach adsorption equilibrium. The suspension was then exposed to a 300 W of high-pressure Hg lamp. A 3 mL of solution was drawn from the system at a certain time interval. After removal of the catalyst by centrifugation, residual RhB concentration was determined through detecting its characteristic adsorption peak intensity at 553 nm on a Shimadzu 2550 UV-visible spectrometer.

## 2.5. Detection of hydroxyl radicals

Hydroxyl radicals ( $\cdot\text{OH}$ ) produced on the surface of  $\text{TiO}_2$  photocatalysts were detected by a photoluminescence (PL) technique. Terephthalic acid was used as the probe molecule due to its easy reaction with  $\cdot\text{OH}$  to produce 2-hydroxyl-terephthalic acid, which had a high fluorescent signal at around 425 nm when excited by 315 nm light.<sup>22-24</sup> The PL intensity of 2-hydroxyl-terephthalic acid was proportional to the amount of  $\cdot\text{OH}$  produced on the surface of  $\text{TiO}_2$  photocatalysts. The experimental procedure was similar to the photocatalytic experiment except using terephthalic acid solution ( $5 \times 10^{-4}$  mol/L) with NaOH concentration of  $2 \times 10^{-3}$  mol/L instead of RhB

solution. The withdrawn solution after centrifugation was measured on a Hitachi F-4500 fluorescence spectrophotometer with the excitation wavelength of 315 nm.

### 3. Results and discussion

#### 3.1. Structures and morphologies of the samples

The composition and crystallinity of the as-prepared samples were analyzed by X-ray diffraction (XRD) and the results were shown in Fig. 1. All the diffraction peaks in Fig. 1 (a-c) can be indexed to tetragonal anatase TiO<sub>2</sub> (JCPDS No.21-1272) and no obvious diffraction peaks are detected for impurities. In addition, Fig. 1c shows the sharpest diffraction peaks with the narrowest half peak width, revealing that the sample prepared with the assistance of H<sub>2</sub>O<sub>2</sub> have higher crystallinity than the other two samples.

Fig. 2 shows the low and high magnification FESEM and TEM images of the as-prepared anatase TiO<sub>2</sub> samples. As presented in Fig. 2a and b, TiO<sub>2</sub> nanorods with diameters of 10-30 nm and lengths of 300-500 nm were obtained hydrothermally with the assistance of both H<sub>2</sub>O<sub>2</sub> and urea. The nanorods have two pointed ends with good dispersion and uniform size, and the sharp contrast between lightness and darkness in Fig. 2c reveals that these nanorods are assembly of small nanoparticles with porous structures. With the assistance of only urea, anatase TiO<sub>2</sub> core-shell nanospheres were formed and they have uniform size with diameters of 300-500 nm as shown in Fig. 2d and e. TEM image in Fig. 2f indicates that core-shell nanospheres are also assembled by nanoparticles. The outer walls have a thickness of around 30-50 nm and the

spacing between the inner and outer walls is about 50 nm. Fig. 2 (g-i) show the TiO<sub>2</sub> microspheres synthesized hydrothermally with the assistance of only H<sub>2</sub>O<sub>2</sub>, which have diameters of 1-2 μm with relatively smooth surfaces.

Fig. 3a shows the TEM image of one randomly selected TiO<sub>2</sub> nanorod and the selected area electron diffraction (SAED) pattern shown in Fig. 3b demonstrates that the nanorod is single crystalline and the pattern can be indexed to the (101), (004) and (105) planes of anatase TiO<sub>2</sub>. The HRTEM image in Fig. 3c clearly shows the crystalline lattice fringes of the TiO<sub>2</sub> nanorod. The two sets of lattices with fringe spacing of 0.35 and 0.48 nm can be assigned to anatase (101) and (002) planes<sup>25, 26</sup>, respectively. The nanorod grows along the [010] direction. Fig. 3d shows a TEM image of the prepared TiO<sub>2</sub> core-shell nanosphere, and its SAED pattern in Fig. 3e exhibits ring patterns which indicates its polycrystalline nature. The diffraction pattern can be indexed to the (101), (004) and (200) planes of anatase TiO<sub>2</sub>. HRTEM image in Fig. 3f confirms the shell is composed of nanoparticles with good crystallinity. A lattice fringe with a spacing of ~0.35 nm can be ascribed to the (101) plane of the anatase-type TiO<sub>2</sub>. Fig. 3g shows a TEM image of the prepared TiO<sub>2</sub> microsphere. The SAED pattern shown in Fig. 3h can be indexed to the (101), (011) and (112) planes of anatase TiO<sub>2</sub> and demonstrates that TiO<sub>2</sub> microspheres are single crystalline. The HRTEM image in Fig. 3i shows the typical (101) crystallographic planes with a lattice space of 0.35 nm.

Nitrogen sorption experiments were undertaken to characterize the specific surface area and porosity of TiO<sub>2</sub> nanorods, TiO<sub>2</sub> core-shell nanospheres and TiO<sub>2</sub>

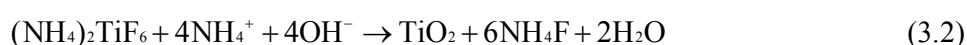
microspheres. The results in Fig. 4 show that the BET surface area of TiO<sub>2</sub> nanorods, TiO<sub>2</sub> core-shell nanospheres, and TiO<sub>2</sub> microspheres is 50.3, 41.9, and 14.9 m<sup>2</sup>/g, respectively. In order to present a clear comparison on the textural properties of the three anatase TiO<sub>2</sub> samples, Table 1 summarizes the data of their specific surface area, average pore size and pore volume. Clearly, TiO<sub>2</sub> nanorods have the largest specific surface area and pore volume while TiO<sub>2</sub> microspheres have the lowest specific surface area and pore volume among the three samples.

### 3.2. Formation mechanism of different TiO<sub>2</sub> architectures

#### TiO<sub>2</sub> core-shell nanospheres prepared hydrothermally with the assistance of urea

In aqueous solution, urea decomposes to create alkaline environment as shown in Eq. 3.1 when the reaction temperature is higher than 80 °C. (NH<sub>4</sub>)<sub>2</sub>TiF<sub>6</sub> begins to hydrolyze as Eq. 3.2 and produces large amounts of low crystalline TiO<sub>2</sub> primary nanoparticles in the solution under the alkaline environment.<sup>27</sup> In order to minimize the surface free energy, these primary nanoparticles tend to agglomerate together to form larger particles. Meanwhile, (NH<sub>4</sub>)<sub>2</sub>TiF<sub>6</sub> concentration decreases as the reaction proceeds and the hydrolysis rate decreases. The variation of crystallite size and crystallinity along the radial direction of the nanoparticles (see Fig. S1) also occurs due to the variation of the hydrolysis and nucleation rate. A classical “Ostwald Ripening” process occurs with the extension of the reaction time, which is recognized as a general formation mechanism of hollow and core-shell nanoparticles.<sup>28</sup> Nanoparticles on the surface of nanospheres have low solubility due to their larger

size and higher crystallinity. They act as the nucleation layer for the subsequent ripening process. Nanoparticles located right underneath of the surface layer are metastable because of their relatively low crystallization and small particle size. They tend to dissolve and recrystallize on the surface, leading to the formation of core-shell structures.



### **TiO<sub>2</sub> microspheres prepared hydrothermally with the assistance of H<sub>2</sub>O<sub>2</sub>**

When H<sub>2</sub>O<sub>2</sub> is added into (NH<sub>4</sub>)<sub>2</sub>TiF<sub>6</sub> solution, the complex of [TiO(H<sub>2</sub>O<sub>2</sub>)]<sup>2+</sup> formed immediately,<sup>29</sup> which suppresses the hydrolysis of (NH<sub>4</sub>)<sub>2</sub>TiF<sub>6</sub>, slows down the nucleation rate of TiO<sub>2</sub> primary nanoparticles, and leads to the formation of grains with larger size and higher crystallinity. As the reaction proceeds, these grains grow into solid microspheres with smooth surfaces due to Ostwald ripening effect.

### **TiO<sub>2</sub> nanorods prepared hydrothermally with the assistance of urea and H<sub>2</sub>O<sub>2</sub>**

Time-dependent experiments were carried out in order to reveal the formation process of anatase TiO<sub>2</sub> nanorods. Typical TEM images of the resultant products are shown in Fig. 5. In the presence of H<sub>2</sub>O<sub>2</sub> and urea, hydrolysis of (NH<sub>4</sub>)<sub>2</sub>TiF<sub>6</sub> and subsequent condensation process took place slowly at the initial stage of the reaction because of the coordinating effect of H<sub>2</sub>O<sub>2</sub> and insufficient decomposition of urea. At 30 min, the monoclinic H<sub>2</sub>Ti<sub>5</sub>O<sub>11</sub>·3H<sub>2</sub>O bundles were first formed and they were assembled by nanosheets with lengths ranging from 50 to 100 nm (see Fig. 5a and Fig. S2a). H<sub>2</sub>Ti<sub>5</sub>O<sub>11</sub>·3H<sub>2</sub>O with a layer structure was formed through the stack of TiO<sub>6</sub>

octahedrons with the assistance of H-O bond.<sup>30, 31</sup> With the increasing reaction time, more OH<sup>-</sup> ions were released from urea. In the alkaline environment, H<sub>2</sub>Ti<sub>5</sub>O<sub>11</sub>·3H<sub>2</sub>O was unstable and preferably transformed into more stable phase with the extension of the time. When the reaction time reached 1 h, some bundles were gradually split to individual nanorods with increased lengths (see Fig. 5b). From the XRD pattern shown in Fig. S2b, H<sub>2</sub>Ti<sub>5</sub>O<sub>11</sub>·3H<sub>2</sub>O nanosheets and anatase TiO<sub>2</sub> nanorods coexisted at this stage, which meant that the morphological variation from 0.5 to 1 h was ascribed to the transformation of monoclinic H<sub>2</sub>Ti<sub>5</sub>O<sub>11</sub>·3H<sub>2</sub>O to tetragonal anatase TiO<sub>2</sub>. With the reaction time increased to 2 h, bundles of nanosheets disappeared and were completely transformed to individual nanorods with diameters of 10-30 nm and lengths up to 300-500 nm (see Fig. 5c). Well-defined nanorods were formed with diameters of 20-40 nm and lengths of 200-300 nm (see Fig. 5d) at 6 h. Oswald ripening contributed to the decrease of aspect ratio of the nanorods from 2 to 6 h.

### **3.3. Photocatalytic activity of TiO<sub>2</sub> nanorods, core-shell nanospheres, and microspheres**

Rhodamine B (RhB) is a common dye with 4 N-ethyl groups at either side of the xanthene ring. It is widely used in industries such as textiles, paper, plastics, tannery, and paints. Wastewater containing RhB can deteriorate water quality and influence the photosynthetic activity of aquatic organisms by imparting the color to the water and impeding the penetration of light in water. In addition, RhB is suspected to be carcinogenic and has adverse effect on human and animal health.<sup>32</sup> Herein, we select Rhodamine B as a model pollutant to investigate the photocatalytic activity of

anatase TiO<sub>2</sub>. In order to evaluate the photocatalytic performances, anatase TiO<sub>2</sub> nanorods, TiO<sub>2</sub> core-shell nanospheres and TiO<sub>2</sub> microspheres were used as the photocatalysts to degrade RhB solution under UV light, respectively. Prior to the irradiation, the adsorption in the dark was conducted so as to reach adsorption equilibrium between the photocatalysts and RhB.<sup>33</sup> The relative concentration of RhB remained nearly unchanged after the time prolonged to 120 min, indicating that adsorption equilibrium had reached between RhB molecules and photocatalysts (see Fig. S3). The final adsorption ratio of anatase TiO<sub>2</sub> nanorods, TiO<sub>2</sub> core-shell nanospheres, and TiO<sub>2</sub> microspheres is 19.0, 16.1, and 11.3 % respectively, which is consistent with their BET surface areas.

Fig. 6 plots the variation of the relative concentration of RhB aqueous solution with the irradiation time. RhB aqueous solution with the initial concentration of  $1 \times 10^{-5}$  mol/L was used to test the photocatalytic performance. As presented, RhB degradation ratio over anatase TiO<sub>2</sub> nanorods can reach 95% merely after 60 min of illumination which is much higher than that over TiO<sub>2</sub> core-shell nanospheres (60%) and TiO<sub>2</sub> microspheres (38%). After 240 min of illumination, RhB degradation ratio over TiO<sub>2</sub> core-shell nanospheres and TiO<sub>2</sub> microspheres can reach 98.0% and 81.9%, respectively. The result shows that anatase TiO<sub>2</sub> nanorods possess much higher photocatalytic activity than TiO<sub>2</sub> core-shell nanospheres and TiO<sub>2</sub> microspheres. For comparison, a blank experiment was conducted under UV light irradiation in the absence of any photocatalyst. The photolysis ratio of RhB is merely 15.1%, manifesting that photocatalysts play a dominant role in the decomposition of RhB

molecules (see Fig. S4).

The kinetics of heterogeneous catalysis of a liquid-solid system has frequently been discussed with Langmuir Hinshelwood (L-H) model,<sup>34, 35</sup> which can be expressed by Eq. 3.3:

$$r = -\frac{dC}{dt} = \frac{k_r KC}{1 + KC + K_s C_s} \quad (3.3)$$

Here,  $C$  is the concentration of the reactant in the solution,  $t$  is the reaction time,  $k_r$  is the reaction rate constant,  $K$  is the adsorption coefficient of the reactant,  $K_s$  is the adsorption coefficient of the solvent, and  $C_s$  is the concentration of the solvent. When the reactant is more strongly adsorbed than solvent, Eq. 3.3 can be simplified to Eq. 3.4.

$$r = -\frac{dC}{dt} = \frac{k_r KC}{1 + KC} \quad (3.4)$$

When the initial concentration of reactant is very low ( $KC \ll 1$ ), Eq. 3.4 can be further simplified to Eq. 3.5, where  $k_{app}$  represents the apparent reaction rate constant.

$$r = -\frac{dC}{dt} = k_r KC = k_{app} C \quad (3.5)$$

Eq. 3.5 can be further written as  $\ln(C/C_0) = k_{app} t$ , where  $C_0$  and  $C$  represent the concentration of RhB at time 0 and  $t$ , respectively. As shown from their kinetic curves (see Fig. S5), a good linear characteristic is presented between  $\ln(C/C_0)$  and reaction time  $t$  for anatase TiO<sub>2</sub> nanorods, TiO<sub>2</sub> core-shell nanospheres and TiO<sub>2</sub> microspheres (0.967, 0.973 and 0.986), respectively. Based on the results in Fig. S5, it is plausible to suggest that the photocatalytic degradation of RhB in the presence of TiO<sub>2</sub> nanorods, TiO<sub>2</sub> core-shell nanospheres, and TiO<sub>2</sub> microspheres follows the simplified L-H model. The apparent reaction rate constant of anatase TiO<sub>2</sub> nanorods, TiO<sub>2</sub> core-shell nanospheres and TiO<sub>2</sub> microspheres is 2.853, 0.294 and 0.0454 h<sup>-1</sup>, indicating that the anatase TiO<sub>2</sub> nanorod sample has higher photocatalytic efficiency than the other samples.

Photocatalytic experiments of anatase TiO<sub>2</sub> nanorods were repeated for four times. The degradation curves of RhB solution with error bars were obtained based on

the performance of four batches of photocatalysts (see Fig. S6). As shown, RhB concentration decreases rapidly with the extension of the irradiation time. The error ranges represented by vertical lines indicate that the photocatalytic performance of photocatalysts fluctuated within narrow range which resulted from distinctions in the activity of TiO<sub>2</sub> nanorods from different batches.

In order to further test the photocatalytic activity of anatase TiO<sub>2</sub> nanorods, the initial concentration of RhB aqueous solution was increased from  $1 \times 10^{-5}$  to  $2 \times 10^{-5}$  and  $5 \times 10^{-5}$  mol/L, and the corresponding results are presented in Fig. S7a and b, which were obtained from the UV-vis spectral variation of RhB aqueous solution with the reaction time (see Fig. S8). After 240 min of illumination, the degradation ratio of RhB ( $2 \times 10^{-5}$  mol/L) is 98.5%. Even at a higher initial concentration ( $5 \times 10^{-5}$  mol/L), the degradation ratio of RhB can still reach 85.9% after 360 min of illumination, which demonstrate that anatase TiO<sub>2</sub> nanorods have good photocatalytic performance for RhB aqueous solution with relatively high concentration.

### 3.4. Light absorption properties

Optical absorption properties of the prepared TiO<sub>2</sub> samples were tested in order to find a possible explanation for their enhanced photocatalytic performance. Fig. 7 shows the diffusion reflectance UV-vis absorption spectra and plot of transformed Kubelka–Munk function versus the energy of the light absorbed of anatase TiO<sub>2</sub> nanorods, TiO<sub>2</sub> core-shell nanospheres and TiO<sub>2</sub> microspheres. As presented in Fig. 7a, TiO<sub>2</sub> nanorods exhibit very similar absorption spectra to TiO<sub>2</sub> core-shell nanospheres.

They both exhibit superior light absorption capacity to TiO<sub>2</sub> microspheres within the wavelength range from 200 to 335 nm because of multiple light reflection and scattering within their porous structures and void space of core-shell architectures. The blue shift for the absorption edges of TiO<sub>2</sub> nanorods and core-shell nanospheres indicates their relatively smaller nanoparticles and larger bandgap in comparison with TiO<sub>2</sub> microspheres.<sup>36</sup> The band gap energies can be determined from the intercepts on the *X* axis in Fig. 7b, which are 2.9, 2.97 and 2.85 eV for TiO<sub>2</sub> nanorods, TiO<sub>2</sub> core-shell nanospheres and TiO<sub>2</sub> microspheres, respectively. The enlarged bandgap and enhanced light absorption capacity is favorable for TiO<sub>2</sub> nanorods and core-shell nanospheres to generate active species ( $\cdot$ OH) for the photocatalytic degradation of RhB.

### 3.5. Characterization of hydroxyl radicals

Active species  $\cdot$ OH radicals generated on the surface of anatase TiO<sub>2</sub> nanorods, TiO<sub>2</sub> core-shell nanospheres and TiO<sub>2</sub> microspheres were probed by terephthalic acid. The reaction between active species  $\cdot$ OH radicals and terephthalic acid has been shown in Fig. 8.<sup>37</sup> As shown in Fig. 9, the PL intensity at around 425 nm increases with the irradiation time, indicating that the amount of  $\cdot$ OH radicals generated on the surface of photocatalysts increases with the time. The sequence of the anatase TiO<sub>2</sub> samples based on the PL intensity detected from high to low is nanorods, core-shell nanospheres and microspheres in turn. The result indicates that TiO<sub>2</sub> nanorods are able to produce more  $\cdot$ OH radicals than TiO<sub>2</sub> core-shell nanospheres and TiO<sub>2</sub>

microspheres. This is possibly because anatase TiO<sub>2</sub> nanorods have larger specific surface areas and pore volume than other two samples which can provide more active sites for the generation of ·OH radicals, thus leading to their higher photocatalytic activity in comparison with other two samples.<sup>38</sup> In Fig. S9, the typical IR spectra in the region 4000-500cm<sup>-1</sup> of the samples are presented. The absorption at 400-700 cm<sup>-1</sup> can be attributed to the Ti–O bond. The band around 3400 cm<sup>-1</sup> is associated with the asymmetric and symmetric stretching vibrations of the –OH group of adsorbed water molecules and the surface hydroxyls of the TiO<sub>2</sub> samples, and that at 1632 cm<sup>-1</sup> is assigned to the bending vibrations of the water molecules. The adsorbed water molecules and hydroxyls on the catalyst surface can react with photo-generated holes on the valent band to form highly reactive hydroxyl radicals, which are beneficial for the decomposition of RhB molecules. Obviously, TiO<sub>2</sub> nanorod sample has the maximum –OH group of adsorbed water molecules and the surface hydroxyls among the three samples, which is benefit to the improvement of photocatalytic activity.<sup>39,40</sup>

### 3.6. Life cycle assessment

Life cycle experiments were conducted to assess the durability of anatase TiO<sub>2</sub> nanorods, and the corresponding results are presented in Fig. 10. The spent photocatalysts were collected, cleaned by deionized water, and dried for reuse after each run. Anatase TiO<sub>2</sub> nanorods were used repeatedly to degrade RhB solution (initial concentration: 1×10<sup>-5</sup> mol/L, 100 mL) under UV light irradiation for 5 times. As

observed, RhB degradation ratio decreases gradually with the increase of the run cycles. After five cycles, RhB degradation ratio can till reach 85.1% over anatase TiO<sub>2</sub> nanorods, indicating their good stability as photocatalysts.

#### 4. Conclusion

A flexible and robust reaction system has been established to respectively prepare TiO<sub>2</sub> nanorods, core-shell nanospheres, and microspheres under the mild hydrothermal conditions merely through adjusting reaction parameters. The as-prepared TiO<sub>2</sub> nanorods have diameters of 10-30 nm and lengths up to 300-500 nm. TiO<sub>2</sub> core-shell nanospheres have diameters of 300-500 nm with an outer wall thickness of 30-50 nm and a 50 nm spacing between the inner and outer walls. The TiO<sub>2</sub> microspheres have diameters of about 1-2 μm. The significant changes in TiO<sub>2</sub> structure and morphology have been achieved through controlling the hydrolysis of (NH<sub>4</sub>)<sub>2</sub>TiF<sub>6</sub> and tuning the nucleation and growth rate of TiO<sub>2</sub> with the assistance of urea and H<sub>2</sub>O<sub>2</sub>. The photocatalytic tests show that anatase TiO<sub>2</sub> nanorods have higher photocatalytic efficiency than TiO<sub>2</sub> core-shell nanospheres and microspheres due to the larger specific area and more ·OH radicals produced. This work opens a low cost, simple and reproducible avenue to large-scale preparation of a variety of micro/nanostructured TiO<sub>2</sub> photocatalysts for applications in environmental remediation.

## Acknowledgments

The authors are grateful to the financial supports of the National Natural Science Foundation of China (NSFC Grants 20976033, 21176054 and 21271058).

## References

1. A. L. Linsebigler, G. Q. Lu and J. T. Yates, Jr., *Chem. Rev.*, 1995, **95**, 735-758.
2. K. Hashimoto, H. Irie and A. Fujishima, *Jpn. J. Appl. Phys.*, 2005, **44**, 8269.
3. C. X. Wang, L. W. Yin, L. Y. Zhang, Y. X. Qi, N. Lun and N. N. Liu, *Langmuir*, 2010, **26**, 12841-12848.
4. J. G. Yu, J. J. Fan and K. L. Lv, *Nanoscale*, 2010, **2**, 2144-2149.
5. W. Shao, F. Gu, C. Z. Li and M. K. Lu, *Inorg. Chem.*, 2010, **49**, 5453-5459.
6. J. H. Cai, Z. Y. Wang, K. L. Lv, Y. Zheng, J. G. Yu and M. Li, *RSC Adv.*, 2013, **3**, 15273-15281.
7. H. Cheng, J. Y. Wang, Y. Z. Zhao and X. J. Han, *RSC Adv.*, 2014, **4**, 47031-47038.
8. C. X. Wang, L. W. Yin, L. Y. Zhang, N. N. Liu, N. Lun and Y. X. Qi, *ACS Appl. Mater. Interfaces*, 2010, **2**, 3373-3377.
9. Z. A. Huang, Z. Y. Wang, K. L. Lv, Y. Zheng and K. J. Deng, *ACS Appl. Mater. Interfaces*, 2013, **5**, 8663-8669.
10. W. X. Zhang, G. D. Chen, Z. H. Yang and C. Y. Zeng, *AIChE J.*, 2013, **59**, 2134-2144.
11. Y. Liu, H. Wang, Y. C. Wang, H. M. Xu, M. Li and H. Shen, *Chem. Commun.*, 2011, **47**, 3790-3792.
12. H. J. Yun, H. Lee, J. B. Joo, W. Kim and J. Yi, *J. Phys. Chem. C*, 2009, **113**, 3050-3055.
13. H. X. Li, Z. F. Bian, J. Zhu, D. Q. Zhang, G. S. Li, Y. N. Huo, H. Li and Y. F.

- Lu, *J. Am. Chem. Soc.*, 2007, **129**, 8406-8407.
14. H. Guo, D. X. Tian, L. X. Liu, Y. P. Wang, Y. Guo and X. J. Yang, *J. Solid State Chem.*, 2013, **201**, 137-143.
  15. M. Zhang, Y. Bando and K. Wada, *J. Mater. Sci. Lett.*, 2001, **20**, 167-170.
  16. H. Yu, J. Pan, Y. Bai, X. Zong, X. Y. Li and L. Z. Wang, *Chem. Eur. J.*, 2013, **19**, 13569-13574.
  17. L. De Marco, M. Manca, R. Giannuzzi, F. Malara, G. Melcarne, G. Ciccarella, I. Zama, R. Cingolani and G. Gigli, *J. Phys. Chem. C*, 2010, **114**, 4228-4236.
  18. Y. M. Cui, L. Liu, B. Li, X. F. Zhou and N. P. Xu, *J. Phys. Chem. C*, 2010, **114**, 2434-2439.
  19. J. Joo, S. G. Kwon, T. Yu, M. Cho, J. Lee, J. Yoon and T. Hyeon, *J. Phys. Chem. B*, 2005, **109**, 15297-15302.
  20. J. N. Nian and H. Teng, *J. Phys. Chem. B*, 2006, **110**, 4193-4198.
  21. B. S. Liu, K. Nakata, M. Sakai, H. Saito, T. Ochiai, T. Murakami, K. Takagi and A. Fujishima, *Langmuir*, 2011, **27**, 8500-8508.
  22. K. I. Ishibashi, A. Fujishima, T. Watanabe and K. Hashimoto, *Electrochem. Commun.*, 2000, **2**, 207-210.
  23. Y. H. He, D. Z. Li, G. C. Xiao, W. Chen, Y. B. Chen, M. Sun, H. J. Huang and X. Z. Fu, *J. Phys. Chem. C.*, 2009, **113**, 5254-5262.
  24. H. F. Cheng, B. B. Huang, Y. Dai, X. Y. Qin and X. Y. Zhang, *Langmuir*, 2010, **26**, 6618-6624.
  25. H. M. Zhang, P. R. Liu, F. Li, H. W. Liu, Y. Wang, S. Q. Zhang, M. X. Guo, H.

- M. Cheng and H. J. Zhao, *Eur. J. Inorg. Chem.*, 2011, **17**, 5949-5957.
26. J. Zhu, S. H. Wang, Z. F. Bian, S. H. Xie, C. L. Cai, J. G. Wang, H. G. Yang and H. X. Li, *CrystEngComm.*, 2010, **12**, 2219-2224.
27. S. H. Liu, X. D. Sun, J. G. Li, X. D. Li, Z. M. Xiu and D. Huo, *Eur. J. Inorg. Chem.*, 2009, **2009**, 1214-1218.
28. H. G. Yang and H. C. Zeng, *J. Phys. Chem. B*, 2004, **108**, 3492-3495.
29. X. X. Li, Y. J. Xiong, Z. Q. Li and Y. Xie, *Inorg. Chem.*, 2006, **45**, 3493-3495.
30. A. Chemseddine and T. Moritz, *Eur. J. Inorg. Chem.*, 1999, **1999**, 235-245.
31. R. L. Penn and J. F. Banfield, *Geochim. Cosmochim. Acta*, 1999, **63**, 1549-1557.
32. T. Y. Li, B. Z. Tian, J. L. Zhang, R. F. Dong, T. T. Wang and F. Yang, *Ind. Eng. Chem. Res.*, 2013, **52**, 6704-6712.
33. S. Zheng, W. J. Jiang, Y. Cai, D. D. Dionysiou and K. E. O'Shea, *Catal. Today*, 2014, **224**, 83-88.
34. X. H. Wang, J. G. Li, H. Kamiyama, Y. Moriyoshi and T. Ishigaki, *J. Phys. Chem. B*, 2006, **110**, 6804-6809.
35. J. Krýsa, G. Waldner, H. Měšt'ánková, J. Jirkovský, G. Grabner, *Appl. Catal., B: Environ.*, 2006, **64**, 290-301.
36. S. Q. Shang, X. L. Jiao and D. R. Chen, *ACS Appl. Mater. Interfaces*, 2012, **4**, 860-865.
37. K. I. Ishibashi, A. Fujishima, T. Watanabe and K. Hashimoto, *Electrochem. Commun.*, 2000, **2**, 207-210.
38. W. J. Jiang, J. A. Joens, D. D. Dionysiou and K. E. O'Shea, *J. Photochem.*

*Photobiol., A: Chem.*, 2013, **262**, 7-13.

39. J. G. Yu, Y. R. Su, B. Cheng and M. H. Zhou, *J. Mol. Catal. A: Chem.*, 2006, **258**, 104-112.
40. J. G. Yu, G. H. Wang, B. Cheng and M. H. Zhou, *Appl. Catal., B: Environ.*, 2007, **69**, 171-180.

### Figure caption

**Fig. 1** XRD patterns of the samples prepared hydrothermally with the assistance of (a) H<sub>2</sub>O<sub>2</sub> and urea, (b) urea, and (c) H<sub>2</sub>O<sub>2</sub> at 180 °C for 2 h.

**Fig. 2** FESEM and TEM images of the samples prepared hydrothermally with the assistance of (a-c) H<sub>2</sub>O<sub>2</sub> and urea, (d-f) urea, and (g-i) H<sub>2</sub>O<sub>2</sub> at 180 °C for 2 h.

**Fig. 3** TEM, SAED, and HRTEM images of (a-c) TiO<sub>2</sub> nanorods, (d-f) TiO<sub>2</sub> core-shell nanospheres, and (g-i) TiO<sub>2</sub> microspheres.

**Fig. 4** N<sub>2</sub> adsorption-desorption isotherms (left) and pore size distribution plots (right) of (a) TiO<sub>2</sub> nanorods, (b) TiO<sub>2</sub> core-shell nanospheres, and (c) TiO<sub>2</sub> microspheres.

**Fig. 5** TEM images of the products prepared hydrothermally with the assistance of urea and H<sub>2</sub>O<sub>2</sub> at different time intervals: (a) 30 min, (b) 1 h, (c) 2 h, and (d) 6 h.

**Fig. 6** Photocatalytic degradation of RhB solution with initial concentration of  $1 \times 10^{-5}$  mol/L under UV light irradiation in the presence of (s1) TiO<sub>2</sub> nanorods, (s2) TiO<sub>2</sub> core-shell nanospheres, (s3) TiO<sub>2</sub> microspheres, and (s4) in the absence of any photocatalyst.

**Fig. 7** Diffuse reflectance UV-vis absorption spectra (a) and plot of transformed Kubelka-Munk function versus the energy of the light absorbed (b) of the samples: (s1) TiO<sub>2</sub> nanorods, (s2) TiO<sub>2</sub> core-shell nanospheres, and (s3) TiO<sub>2</sub> microspheres.

**Fig. 8** The reaction between ·OH radicals and terephthalic acid.

**Fig. 9** Fluorescence spectral changes of terephthalic acid solution under UV light irradiation in the presence of (a) TiO<sub>2</sub> nanorods, (b) TiO<sub>2</sub> core-shell nanospheres, and

(c) TiO<sub>2</sub> microspheres.

**Fig. 10** Life cycle performance of TiO<sub>2</sub> nanorods in the photocatalytic degradation of RhB solution ( $1 \times 10^{-5}$  mol/L) under UV light irradiation.

**Table 1.** Textural properties of TiO<sub>2</sub> nanorods, core-shell nanospheres, and microspheres.

Fig. 1

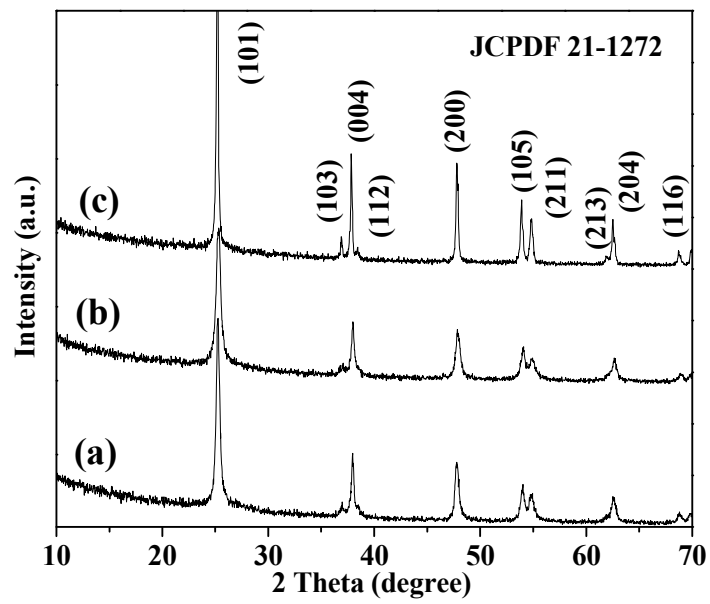


Fig. 2

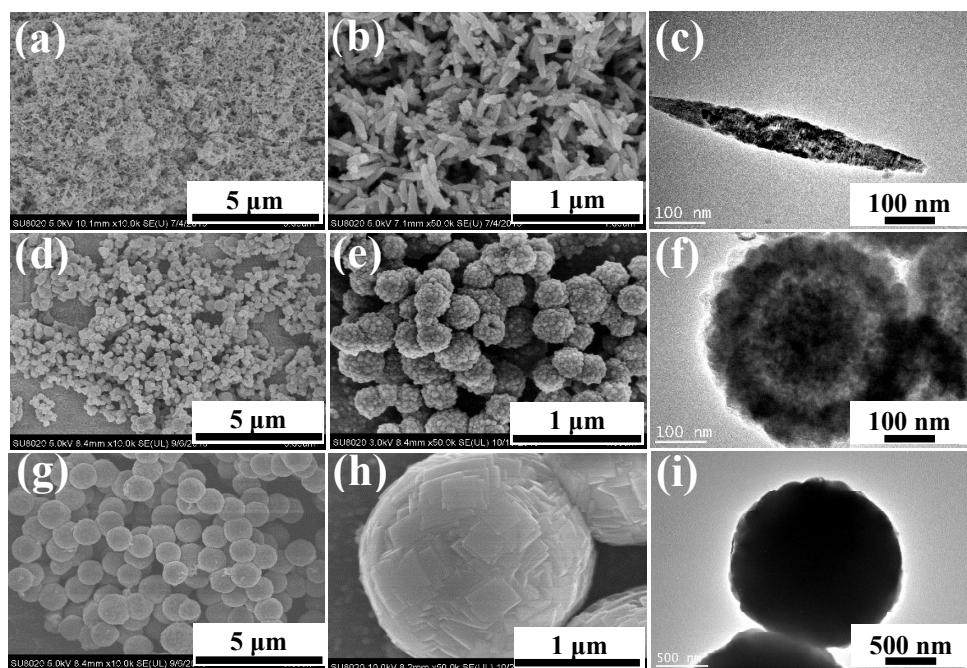


Fig. 3

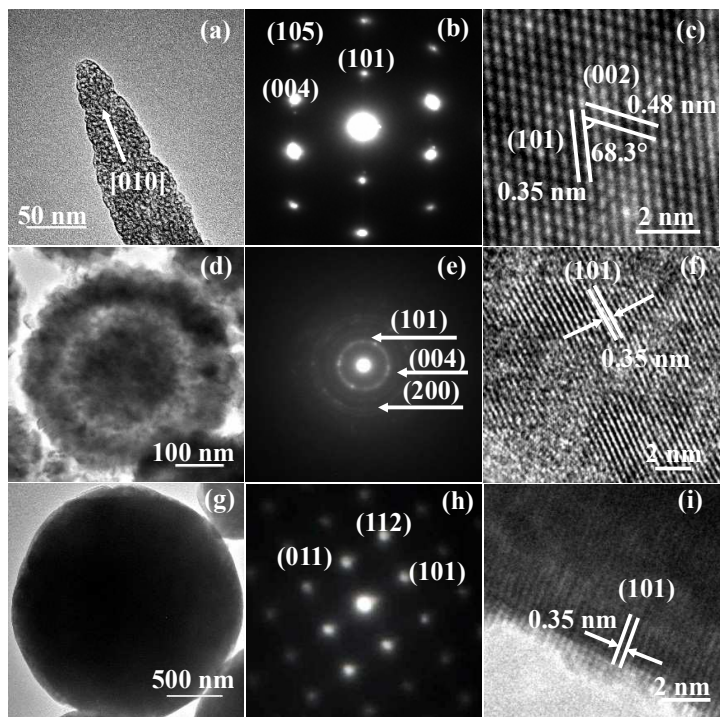


Fig. 4

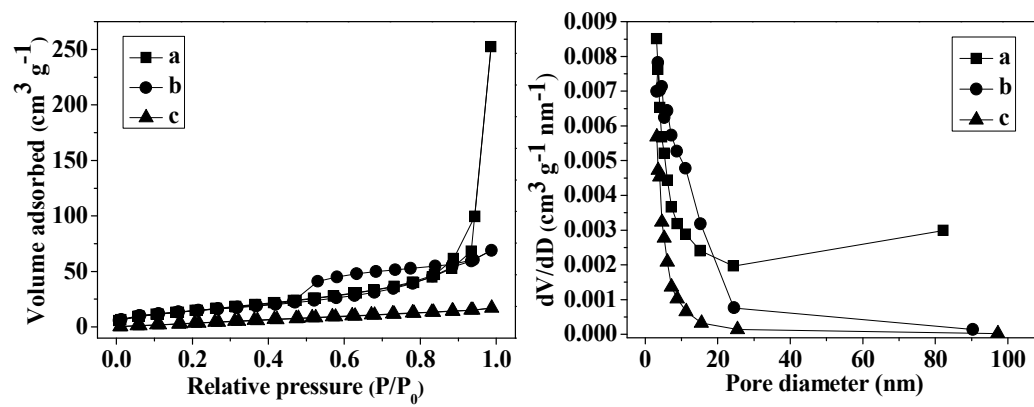


Fig. 5

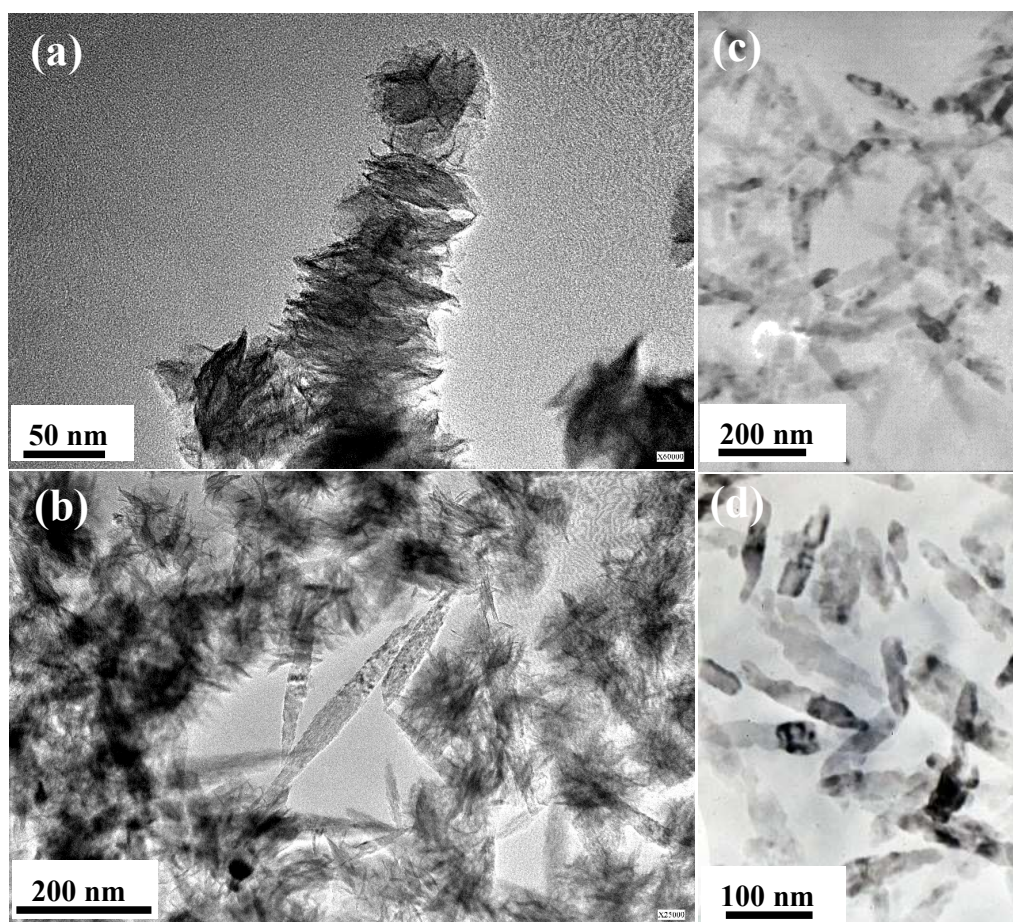


Fig. 6

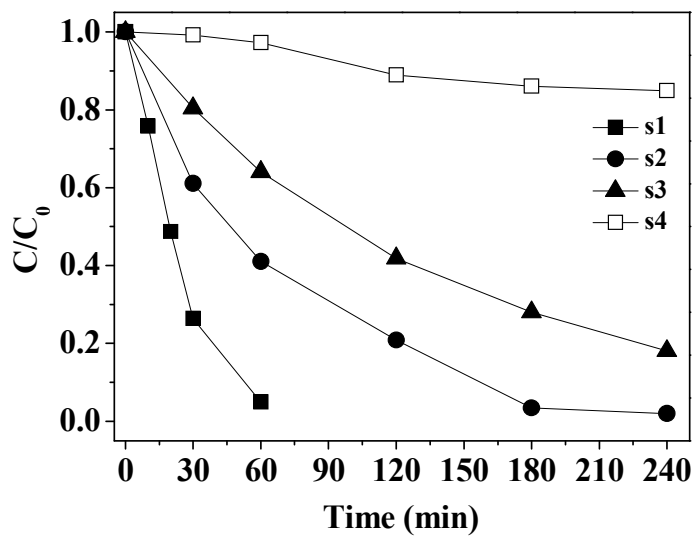


Fig. 7

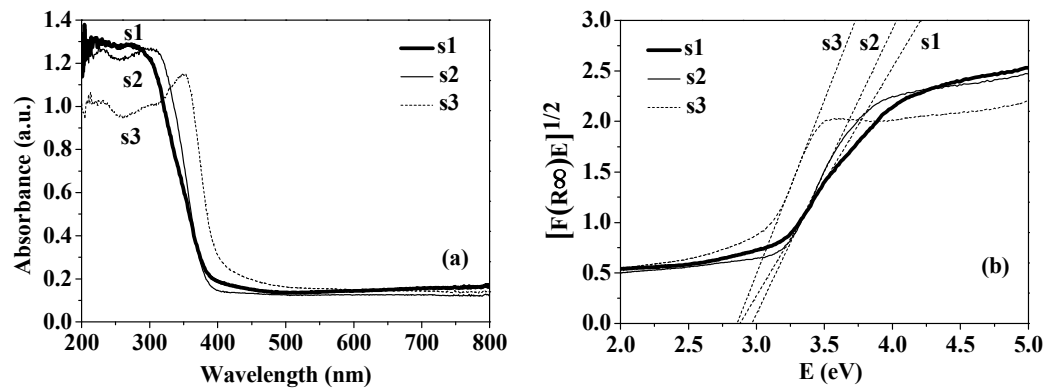


Fig. 8

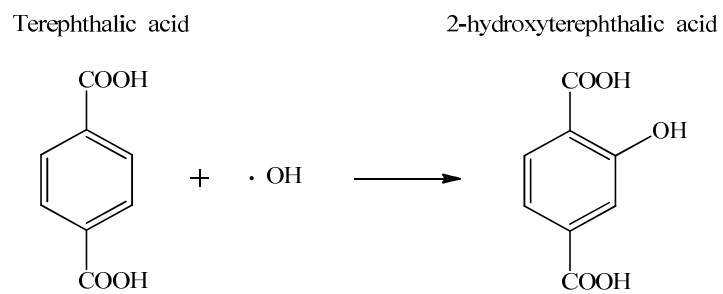


Fig. 9

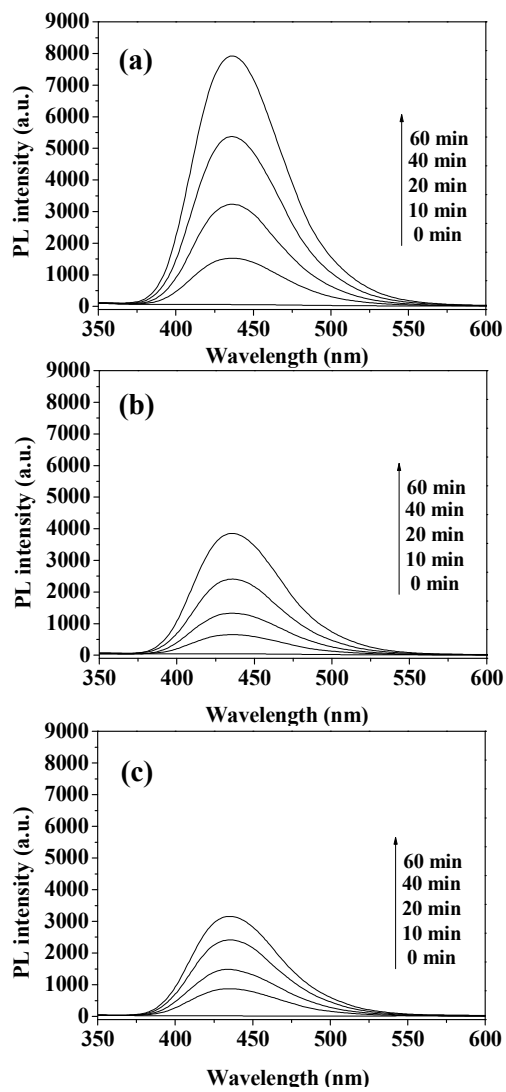
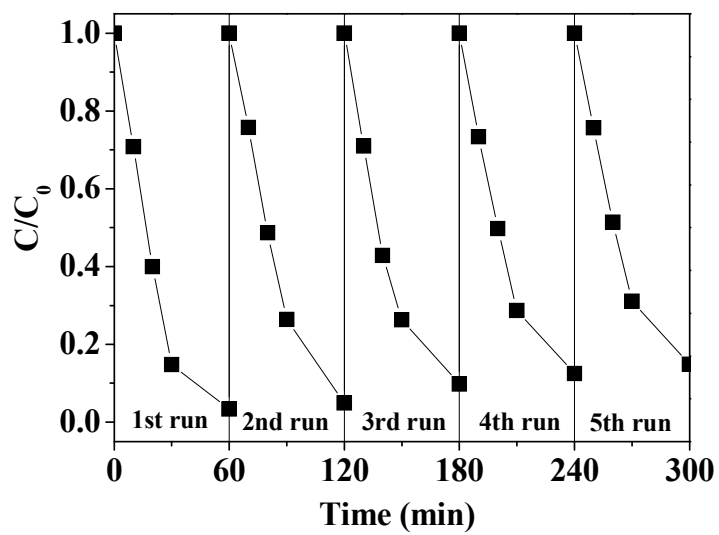


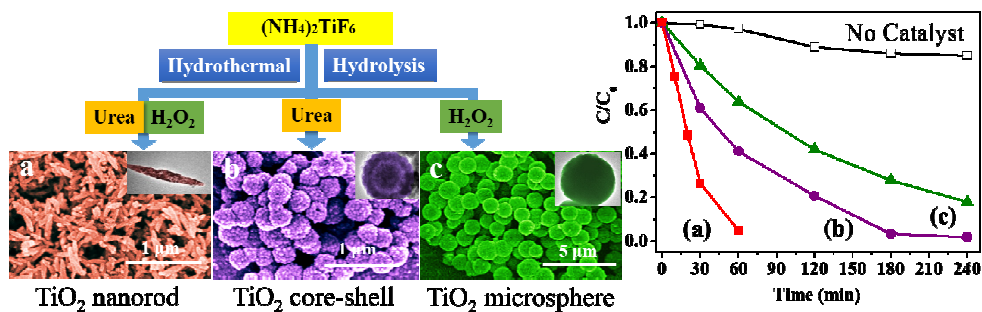
Fig. 10



**Table 1**

Sample	Specific surface area (m <sup>2</sup> /g)	Average pore size (nm)	Pore volume (cm <sup>3</sup> /g)
TiO <sub>2</sub> nanorods	50.3	3.17	0.385
TiO <sub>2</sub> core-shell nanospheres	41.9	3.57	0.098
TiO <sub>2</sub> microspheres	14.9	3.21	0.024

## Graphical Abstract



TiO<sub>2</sub> nanorods, core-shell nanospheres, and microspheres have been respectively prepared through controlling hydrolysis and nucleation rate of Ti<sup>4+</sup> ions in the (NH<sub>4</sub>)<sub>2</sub>TiF<sub>6</sub> aqueous solution in the presence of urea and/or H<sub>2</sub>O<sub>2</sub> by a simple hydrothermal method. The photocatalytic tests demonstrate that anatase TiO<sub>2</sub> nanorods have higher photocatalytic efficiency than TiO<sub>2</sub> core-shell nanospheres and microspheres due to the larger specific area and more ·OH radicals produced. Our work provides a new insight for improving photocatalytic performance of TiO<sub>2</sub> through morphological engineering, which will expect potential applications in environmental remediation.